Dual boundary element assessment of three-dimensional fatigue crack growth

Adrián P. Cisilino[a,*], M.H. Aliabadi[b]

[a]*Universidad Nacional de Mar del Plata, Welding and Fracture, Division-INTEMA, CONICET, Av. Juan B. Justo 4302, Mar del Plata 7600, Argentina*
[b]*Department of Engineering, Queen Mar, University of London, London, UK*

Abstract

In this paper a general procedure for the analysis of three-dimensional multiple fatigue crack growth is presented. The crack propagation is simulated using an incremental crack extension analysis based on the strain energy density criterion and the Paris law. For each crack extension the dual boundary element method is used to perform single region analysis of the cracked component. Stress intensity factors are computed along the crack fronts using a displacement-based method. Crack extensions are automatically modelled with the introduction of new boundary elements along the crack fronts and a localized rediscretization in the area where the cracks intersect the free surfaces. The capability of the procedure is demonstrated by solving a number of multiple edge-crack examples. Results are compared with experimental observations.

© 2004 Elsevier Ltd. All rights reserved.

Keywords: Fatigue crack growth; Dual Boundary Element Method

1. Introduction

The problem of fatigue crack propagation is of major concern in the design of structures for use in engineering applications, making the prediction of crack growth a challenging problem for structural engineers It is important to give an accurate estimate of the life expectancy of mechanical and structural components that can be expressed in a number of fatigue cycles. Normally, trained technicians can detect cracks. Cracks up to a certain size are accepted and are, in fact, allowed in the initial design of the component by making use of the concept of damage tolerance.

The problem is further complicated if crack interaction is considered. Weld joints are typical cases in which the fatigue crack interaction phenomena arise. In welded components initial defects are associated with the fusion and solidification process (cracking, metallurgical transformations, residual stress, inclusions, etc.) and they are located in a zone which usually has a high level of stress induced y the geometric discontinuity of the weld toe. Due to the periodicity in the geometry of the weld toe (specially for automatic welding), crack initiation points are regularly distributed along the weld toe, resulting in the formation of similar periodic arrays of cracks. Experimental and theoretical results demonstrate that the rate at which small cracks initiate and propagate is strongly dependent on crack interaction, microstructural characteristics and residual stress [1,2]. Propagation and coalescence of these initial cracks could lead to the formation of a dominant crack, such that subsequent propagation could result the failure or instability of the component.

The different ways in which cracks interact depend primarily on their spatial distribution, applied stresses and the problem geometry. Although there have been some advances in the fracture mechanics theory of crack interaction, it appears that there is still insufficient knowledge to treat this problem with confidence. To simplify assessment of such defects, a hypothetical simplified bounding shape is often used. This is known as 'recharacterization'. The ASME Code Section XI [3] and the BSI PD6493 Code [4] propose a number of rules for the recharacterization and the analysis of crack interaction and coalescence problems. However, these recharacterization

* Corresponding author. Tel.: +54-223-4816600; fax: +54-223-4810046.

E-mail address: cisilino@fi.mdp.edu.ar (A.P. Cisilino).

procedures follow mostly empirical rules which can vary significantly among different codes, as it was shown by Tu and Dai [5].

While it is absolutely vital to perform experiments and mathematical analysis in order to assess the problem of multiple fatigue crack interaction, it is also necessary to develop numerical schemes, which allow the engineer to apply the devised methods to real problems. During the last decades numerical methods have emerged as powerful and reliable tools to assess problems involving cracks. In this sense its is worth to mention the inclusion of numerical modelling as recommended analysis tool in the recent Fitness-for-Purpose assessment procedure of the API 579 [6].

The simulation of general mixed-mode crack growth using numerical techniques requires the capability of predicting the direction and amount of crack growth, as well as the robustness to update the numerical model to account for the changing crack geometry. It is in this last aspect of the problem that the BEM presents an important advantage when compared to domain methods as FEM. An intrinsic feature common to all domain formulations is the need for continuous internal remeshing to follow the crack propagation, sometimes making automatic remeshing a difficult task. On the other hand the BEM, and in particular its dual formulation (the Dual Boundary Element Method or DBEM), dramatically facilitates the remeshing task, as it is limited to the crack front only.

In this paper the DBEM is presented to model fatigue crack propagation using an incremental crack extension analysis based on the strain energy density criterion and the Paris law. Also presented is an automatic remeshing procedure, which accommodates model changes in the original system matrices and allows important savings in computing time.

2. The dual boundary element method for three-dimensional problems

2.1. Boundary element formulation

The mathematical degeneration of the BEM when applied to crack problems, where the two crack surfaces are considered coplanar was shown by Cruse [7]. Some special techniques have been devised to overcome this difficulty. Among these, the most general is the DBEM introduced by Portela et al. [8]. The DBEM incorporates two independent boundary integral equations, with the displacement equation applied for collocation on one of the crack surfaces and the traction equation on the other. Consider a body with domain $\Omega(X)$ surrounded by a boundary $\Gamma(x)$ which in general can be divided into three surfaces: $\Gamma^+(x)_a$ and $\Gamma^-(x)$, which are the two coincident crack surfaces, and $\Gamma^e(x)$, which is the remaining surface such that $\Gamma(x) = \Gamma^e(x) + \Gamma^+(x) + \Gamma^-(x)$ (see Fig. 1).
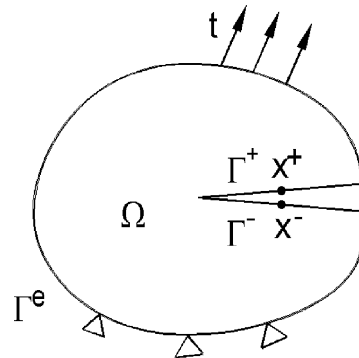

Fig. 1. Model boundary division.

The displacement boundary integral equation relating the boundary displacements $u_j(x)$ with the boundary tractions $t_j(x)$ in the absence of body forces can be written as,

$$c_{ij}(x')u_i(x') + \fint_\Gamma t^*_{ij}(x',x)u_j(x)\,\mathrm{d}\Gamma(x) = \int_\Gamma u^*_{ij}(x',x)t_j(x)\,\mathrm{d}\Gamma(x)$$

(1)

where i,j denote Cartesian components; and $tt^*_{ij}(x',x)$ and $u^*_{ij}(x',x)$ represent the traction and displacement fundamental solutions at a boundary point x due to a unit load placed at location x'. The symbol $\fint$ denotes Cauchy principal value integral, and its existence is guaranteed if the displacement field is Hölder continuous. The term $c_{ij}(x')$ is generally a function of the geometry variation at the boundary point x'. Providing that x' is a smooth boundary point, that is, the outward normal vector to the boundary is continuous at x', then it can be shown that $c_{ij}(x') = 1/2\delta_{ij}$ [9]. Expression for the fundamental solutions $t^*_{ij}(x',x)$ and $u^*_{ij}(x',x)$ are given in the Appendix A.

Assuming continuity of both strains and tractions at x' on a smooth boundary, the boundary traction integral equation is obtained by differentiating Eq. (1) and applying the material constitutive relationships [9]

$$\frac{1}{2}t_i(x') + n_i(x')\fint_\Gamma T^*_{ijk}(x',x)u_k(x)\,\mathrm{d}\Gamma(x)$$

$$= n_i(x')\fint_\Gamma U^*_{ijk}(x',x)t_k(x)\,\mathrm{d}\Gamma(x)$$

(2)

where $n_i(x')$ denotes the component of the outward unit normal to the boundary at x'. The kernels $T^*_{ijk}(x',x)$ and $U^*_{ijk}(x',x)$ contain derivatives of $t^*_{ij}(x',x)$ and $u^*_{ij}(x',x)$ together with elastic constants. The symbol $\fint\!\!\!=$ denotes Hadamard principal value integral. The factor 1/2 multiplying the traction component $t_i(x')$ corresponds to the jump on the displacement derivatives and on the tractions due to the limiting process. This factor is the traction counterpart to the term $c_{ij}(x')$ appearing in the displacement integral equation. The boundary integral Eqs. (1) and (2) constitute the DBEM. Expressions for the fundamental solutions $T^*_{ijk}(x',x)$ and $U^*_{ijk}(x',x)$ can be found in the Appendix.

The number of unknowns involved in the DBEM formulation can be reduced by writing Eqs. (1) and (2)

in terms of the crack opening and sliding displacements (see Aliabadi and Rooke [10]). Thus, the displacement Eq. (1) can be re-written using a simplified notation as

$$c_{ij}(x')u_i(x') + \oint_{\Gamma^e} t_{ij}^* u_j \, \mathrm{d}\Gamma + \oint_{\Gamma^+} t_{ij}^* u_j \, \mathrm{d}\Gamma + \oint_{\Gamma^-} t_{ij}^* u_j \, \mathrm{d}\Gamma$$

$$= \int_{\Gamma^e} u_{ij}^* t_j \, \mathrm{d}\Gamma + \int_{\Gamma^+} u_{ij}^* t_j \, \mathrm{d}\Gamma + \int_{\Gamma^-} u_{ij}^* t_j \, \mathrm{d}\Gamma \qquad (3)$$

For the case of traction-free crack surfaces and considering the property of the traction kernel that $t_{ij}^{*+} = -t_{ij}^{*-}$, expression (3) results in

$$c_{ij}(x')u_i(x') + \oint_{\Gamma^e} t_{ij}^* u_j \, \mathrm{d}\Gamma + \oint_{\Gamma^+} t_{ij}^* \Delta u_j \, \mathrm{d}\Gamma = \int_{\Gamma^e} u_{ij}^* t_j \, \mathrm{d}\Gamma \qquad (4)$$

where the new unknowns are given by $\Delta u_j = u_j^+ - u_j^-$. A similar expression can be obtained for the traction Eq. (2), considering in this case that $T_{ijk}^{*+} = -T_{ijk}^{*-}$:

$$\frac{1}{2} t_i(x') + n_i(x') \fint_{\Gamma^e} T_{ijk}^* u_k \, \mathrm{d}\Gamma + n_i(x') + \fint_{\Gamma^+} T_{ijk}^* \Delta u_k \, \mathrm{d}\Gamma$$

$$= n_i(x') \oint_{\Gamma^e} U_{ijk}^* t_k \, \mathrm{d}\Gamma \qquad (5)$$

Eqs. (4) and (5) constitute the expressions of the EPDBEM when the relative displacements between the crack surfaces are introduced as unknowns.

2.2. Modelling and discretization strategy

Because of the continuity requirements in the displacement and traction fields for the existence of the traction boundary integral equation, special considerations have to be taken into account regarding the modeling and discretization strategies The one used in this work is similar to that proposed initially proposed for two dimensional problems by Portela et al. [8] and later extended to three-dimensional problems by Mi and Aliabadi [11] and Cisilino and Aliabadi [12]. It can be summarized as follows (see Fig. 2):

- Only one of the crack surfaces is discretized, and the traction boundary integral Eq. (5) is applied for collocation. The discretization is done using discontinuous 9-noded quadratic elements (see Fig. 3(a)). Special elements are placed on the crack front to reproduce the r variation in the displacement field at the crack tip.
- Continuous 9-noded quadratic elements are used over the remaining boundary of the model, except at the intersection of a crack and a boundary surface. In these regions edge discontinuous elements (see Fig. 3(b)) are employed to avoid a common node at the intersection. The displacement integral Eq. (4) is used to collocate in both cases.
- Discontinuous 6-noded triangular elements are used during the propagation process for the rediscretization of those regions of the boundary where cracks intersect free
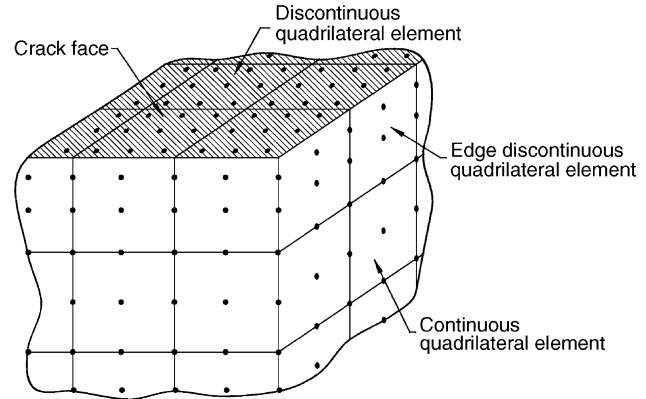

Fig. 2. Discretization strategy.

surfaces. In order to do this a local automatic remeshing strategy has been devised. A detailed description of the remeshing procedure will be given in Section 4.2.

This simple strategy is robust and allows the DBEM effectively to model general edge crack problems. Crack tips, crack edge corners and crack kinks o not require special treatment since they are not located at nodal points here collocation is carried out. The expressions for the shape functions for the different elements can be found in Ref. [13]

2.3. Discretized DBEM Expressions

Following the standard procedures the expressions for the discretized equations for the DBEM can be obtained from Eqs (4) and (5). In a compact form they are given by

$$\mathbf{c}(x')\mathbf{u}(x') + \sum_{n=1}^{N_e} \left(\int_{\Gamma_n} \mathbf{t}^* \mathbf{\Psi}^T \, \mathrm{d}\Gamma \right) \mathbf{u}^n + \sum_{n=1}^{N_c} \left(\int_{\Gamma_n} \mathbf{t}^* \mathbf{\Psi}^T \, \mathrm{d}\Gamma \right) \Delta \mathbf{u}^n$$

$$= \sum_{n=1}^{N_e} \left(\int_{\Gamma_n} \mathbf{u}^* \mathbf{\Psi}^T \, \mathrm{d}\Gamma \right) \mathbf{t}^n \qquad (6)$$

for the displacement boundary integral Eq. (4) and

$$\mathbf{t}(x^-) + \sum_{n=1}^{N_e} \mathbf{n}(x^-) \left(\int_{\Gamma_n} \mathbf{T}^* \mathbf{\Psi}^T \, \mathrm{d}\Gamma \right) \mathbf{u}^n$$

$$+ \sum_{n=1}^{N_c} \mathbf{n}(x^-) \left(\int_{\Gamma_n} \mathbf{T}^* \mathbf{\Psi}^T \, \mathrm{d}\Gamma \right) \Delta \mathbf{u}^n$$

$$= \sum_{n=1}^{N_e} \mathbf{n}(x^-) \left(\int_{\Gamma_n} \mathbf{U}^* \mathbf{\Psi}^T \, \mathrm{d}\Gamma \right) \mathbf{t}^n \qquad (7)$$

for the traction integral Eq. (5). In these equations N_e and N_c are the number of elements used in the discretization of the external boundary Γ^e and the crack surface Γ^c, respectively, while $\mathbf{c}, \mathbf{u}^*, \mathbf{U}^*$ and $\mathbf{T}^*$ denote 3×3 submatrices resulting from the consideration of the Cartesian components; $\mathbf{u}, \Delta \mathbf{u}$, ant $\mathbf{t}$ are 3×1 vectors, and $\mathbf{\psi}$ is a vector containing the shape functions. The dimension of vector $\mathbf{\psi}$ is 6×1 or 9×1 depending on whether the element under consideration is triangular or quadrilateral.
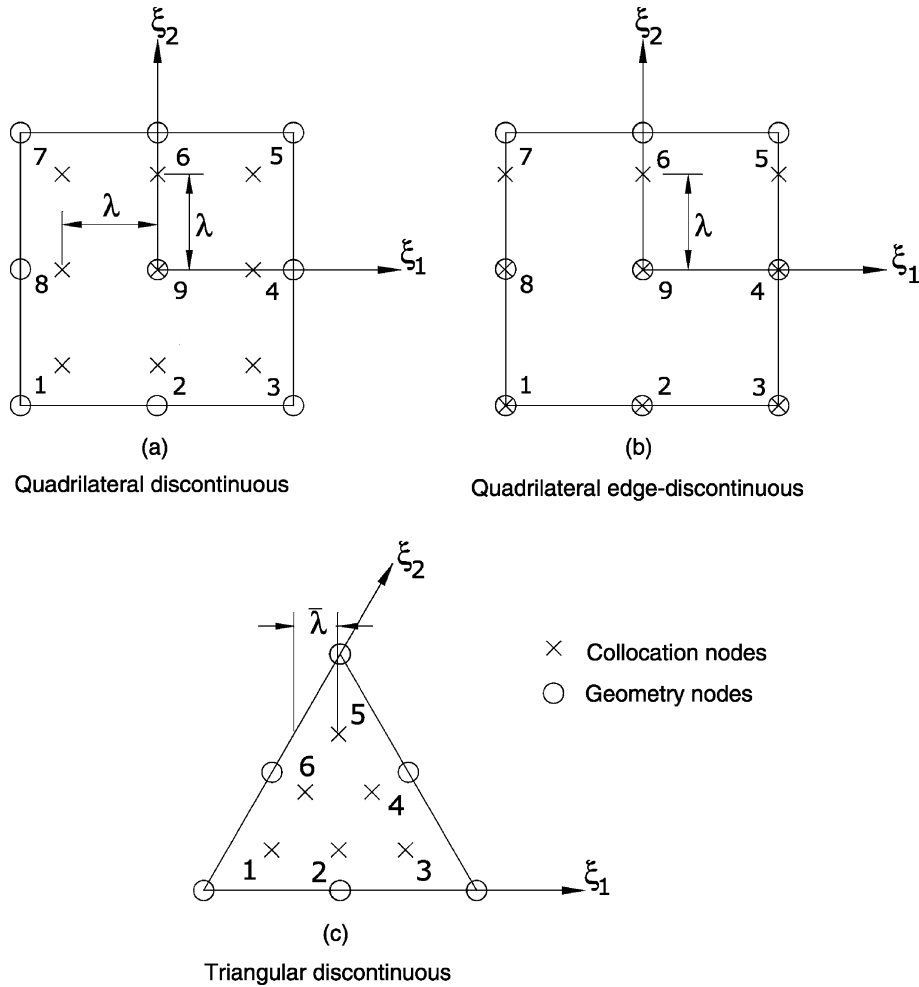
Fig. 3. Discontinuous and edge-discontinuous elements.

After the collocation point passes through all the collocation nodes, Eqs. (6) and (7) give a system of linear equations, which can be expressed in a matrix form as

$$\mathbf{Hu} = \mathbf{Gt} \tag{8}$$

where matrix $\mathbf{H}$ contains integrals involving t_{ij}^* and T_{ij}^*, and matrix $\mathbf{G}$ contains integrals involving u_{ij}^* and U_{ij}^*. Vectors $\mathbf{u}$ and $\mathbf{t}$ consist of all nodal displacements and traction components on the boundary. Rearranging Eq. (8) according to the boundary conditions results in

$$\mathbf{Ax} = \mathbf{By} = \mathbf{f} \tag{9}$$

where $\mathbf{x}$ is the vector containing the boundary unknowns u_i, t_i and Δu_i, and $\mathbf{f}$ is the vector for known components (boundary conditions). All boundary nodal values of u_i, t_i and Δu_i become known after solving Eq. (9).

2.4. Treatment of the Integrals

The problem of the evaluation of singular integrals has been encountered since the beginning of the BEM Efficient and accurate evaluation of singular integrals is critical for

the performance of the boundary element formulation. According to the nature of the kernel, and the relative position of the collocation point with respect to the element on which the integration is carried out, four kinds of integrals can be identified in the DBEM presented in this work:

- *Nearly singular integrals*: This term is used to define integrals which are not singular, but have integrands which vary sharply as the source point approaches the integration element. This applies to all kernel functions, provided that the collocation point does not lie within the integration element. They are evaluated using standard Gauss quadrature formulae with an element subdivision technique as in Lachat and Watson [14].
- *Singular integrals*: This type of singular integral appears when the collocation node lies within the integration element and the singularity of the kernel is of order $1/r$. This applies to kernel the function $u_{ij}^*(x', x)$. Effective methods for the evaluation of these integrals are those based on variable transformation, as the polar coordinate transformation due to Rizzo and Shippy [15]

and the triangle to square transformation due to Lachat and Watson [14].

- *Strongly singular integrals*: Integrals involving kernel functions presenting a singularity of order $1/r^2$ are denoted as strongly singular. The kernel functions $t_{ij}^*(x', x)$ and $U_{ijk}^*(x', x)$ present this type of singularity. Two different situations have to be considered when evaluating strongly singular integrals. The transformation of variable described in the previous item can be used to reduce the $1/r^2$ singularity to improve the accuracy of the so-called off-diagonal terms, i.e. when the collocation point x' is on the integration element but the shape function $\psi_i = 0$ at x'. On the other hand, the strongly singular traction integral where $\psi_i = 1$ at x' can be indirectly obtained from body motion considerations [9].

- *Hyper-singular integrals*: This term is used to define integrals of kernel functions that present singularities of order $1/r^3$. This applies to the kernel function $T_{ijk}^*(x', x)$. Hyper-singular integrals can be evaluated employing a technique developed by Guiggiani et al. [16] who utilized a singularity subtraction technique using series expansions developed by Aliabadi et al. [17]. Details of its implementation to DBEM problems can be found in Mi and Aliabadi [18].

3. Fatigue crack propagation

The presence of cyclic loads on a flawed structure or component can lead to an increase in crack length at each step, even though the maximum stress intensity factor may be much less than the critical one. By characterizing fatigue crack growth using linear elastic fracture mechanics parameters, it is possible to predict crack growth rates under cyclic loading.

3.1. Crack extension

Fig. 4 is a schematic log–log plot of the rate of crack growth per load cycle, da/dN, as a function of the applied stress intensity factor range, $\Delta K = K_{max} - K_{min}$, depicted in Fig. 5. The sigmoidal curve contains three distinct regions. In the first region, crack growth goes asymptotically to zero as ΔK approaches a threshold value ΔK_{th}. This means that for stress intensity factors below ΔK_{th} there is no crack growth, i.e. there is a fatigue limit. The threshold effect is believed to be caused by a number of different processes, which lead to crack blocking. In region II, the log da/dN tends to vary linearly with respect to the log of ΔK, finally to accelerate dramatically in region III as ΔK approaches K_c, the fracture toughness of the material.

Paris et al. [19] developed an empirical formula which relates the rate of growth per load cycle, da/dN, to the stress
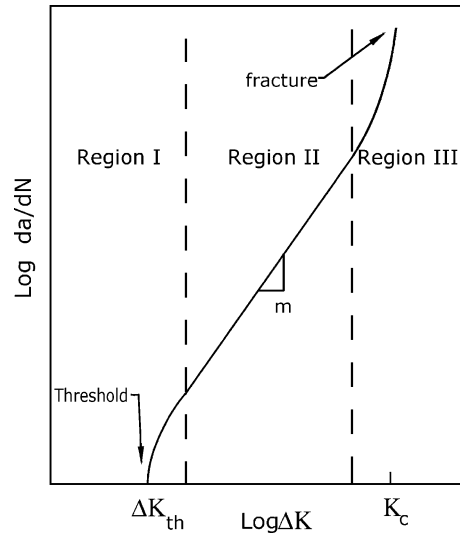

Fig. 4. Typical fatigue crack growth behaviour in metals.

intensity factor range ΔK in the linear region

$$\frac{\mathrm{d}a}{\mathrm{d}N} = C\Delta K^n \tag{10}$$

where C and n are empirical material constants which may also depend on load frequency, environment and mean load. Eq. (10) is normally called the Paris law, and has gained acceptance in engineering practice.

3.2. Criteria for crack growth direction

There is no unique criterion regarding crack growth direction. Many theories and hypotheses have been suggested [20]. Among them the minimum strain energy density criterion, or S-criterion is selected for this work. The S-Criterion, was formulated by Sih [20]. It states that
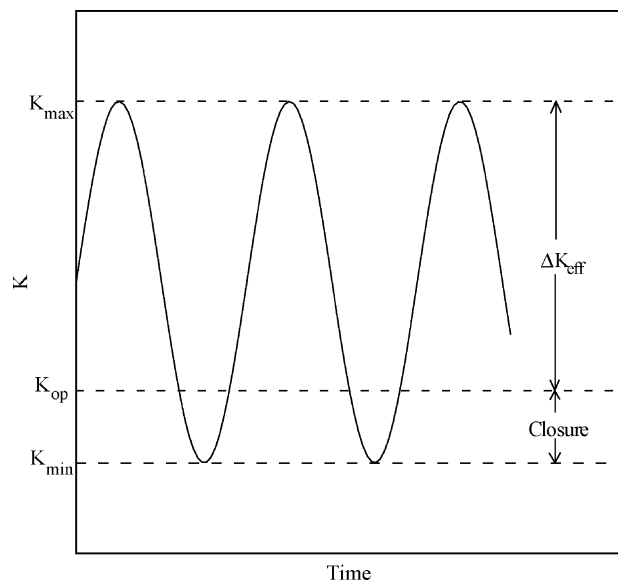

Fig. 5. Definition of stress intensity range.

the direction of crack growth at any point along the crack front is towards the region with the minimum value of strain density factor S. In terms of the of the stress intensity factors K_I, K_{II} and K_{III} can be written as

$$S(\theta) = a_{11}(\theta)K_I^2 + 2a_{12}(\theta)K_I K_{II} + a_{22}(\theta)K_{II}^2 + a_{33}(\theta)K_{III}^2 \tag{11}$$

where

$$a_{11} = \frac{1}{16\pi\mu}(3 - 4\nu - \cos\theta)(1 + \cos\theta)$$

$$a_{12} = \frac{1}{8\pi\mu}\sin\theta(\cos\theta - 1 + 2\nu)$$

$$a_{22} = \frac{1}{16\pi\mu}[4(1 - \nu)(1 - \cos\theta) + (3\cos\theta - 1)(1 + \cos\theta)]$$

$$a_{33} = \frac{1}{4\pi\mu} \tag{12}$$

in which μ is the shear modulus of elasticity and ν the Poisson's ratio.

The derivative of $S(\theta)$ with respect to θ can be obtained from expression (11), and the stationary point of $S(\theta)$ calculated by solving

$$\frac{dS(\theta)}{d\theta} = 0, \qquad -\pi < \theta < \pi \tag{13}$$

Finally, S_{min} is obtained by comparing the values of $S(\theta)$ at stationary points $d^2S(\theta)/d\theta^2 > 0$.

3.3. Crack closure

Soon after he Paris law (10) gained wide acceptance as a fatigue crack growth criterion, many researchers came to the realization that this simple expression was not universally applicable, as experimental evidence showed that fatigue crack growth rates exhibit a dependence on the load ratio $R = K_{min}/K_{max}$.

A discovery by Elber [21] provided at least a partial explanation for the R effect. Elber postulated that crack closure decreased the fatigue crack growth rate by reducing the effective stress intensity range. Fig. 5 shows the closure concept. When a specimen is cyclically loaded between K_{max} and K_{min}, the crack faces are in contact below K_{op}, the stress intensity at which the crack opens. Elber assumed that the portion of the cycle which is below K_{op} does not contribute to fatigue crack growth. He defined an effective stress intensity range as follows:

$$\Delta K_{eff} = K_{max} - K_{op} \tag{14}$$

and also introduced an effective stress intensity ratio:

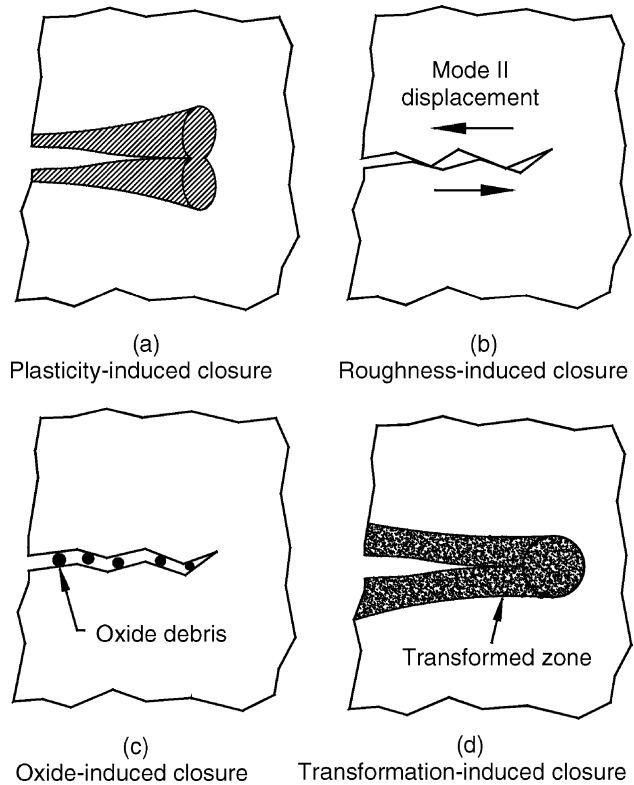$$U = \frac{\Delta K_{eff}}{\Delta K} = \frac{K_{max} - K_{op}}{K_{max} - K_{min}} \tag{15}$$

Fig. 6. Fatigue crack closure mechanisms.

Elber also proposed a modified Paris law equation:

$$\frac{da}{dN} = C(\Delta K_{eff})^n \tag{16}$$

Eq. (16) has been reasonably successful in correlating fatigue crack growth data at various R ratios.

Since Elber's original study, numerous researchers have confirmed that crack closure does in fact occur during fatigue crack propagation. Many mechanisms have been identified for fatigue crack closure; some of them are shown in Fig. 6. Plasticity-induced closure, Fig. (a), results from residual stresses in the plastic wake, while roughness-induced closure, which is shown in Fig. 6(b), is influenced by microstructure. Oxide-induced closure, Fig. 6(c), is usually associated with an aggressive environment. In this mechanism, oxide debris or rather corrosion products act as a wedge between crack faces. Another mechanism is given by a stress-induced martensitic transformation at the tip of the growing crack (see Fig. 6(d)), which results in a process zone where residual compressive stresses can lead to crack closure.

4. Crack propagation analysis

In what follows, a numerical procedure for fatigue crack growth modeling will be introduced The proposed procedure involves an incremental crack extension analysis

based on the minimum strain energy criterion and the Paris law. In the first stage the initial crack geometries are defined, and the BEM is applied to perform a stress analysis and to calculate the stress intensity factors along the crack front. The direction of the incremental extension is then determined using the minimum strain energy criterion, while the Paris law is employed to calculate the size of the extension. The incremental extension of the cracks is modelled by adding new elements at their fronts, together with an automatic localized remeshing in those regions where cracks intersect free surfaces (noted here as tip areas). A new boundary element solution is then carried out for the new configuration and the process is repeated. The above incremental analysis is performed until the predefined crack length is reached.

4.1. Stress intensity factor computation

The relative displacements of the crack surfaces Δu calculated from the boundary element analysis are used in the near crack tip stress field equations to obtain the local mixed-mode stress intensity factors. Three sets of stress intensity factors are computed on each element along the crack front (points Q in Fig. 7), by using the relative displacements Δu^P of the second row of collocation nodes. These points are referred to from now on as points P (see Fig. 7).

For any point P located on the crack surface, point Q is given by the position where a section plane orthogonal to the plane of the crack and containing point P is normal to the tangent to the crack front. It is clear that the positions of points Q depend on the local geometry of the crack front, and have to be determined in each case. Since the crack front geometry is given by mapping the local intrinsic coordinates of the elements (ξ_1, ξ_2) into the global coordinate system, the positions of points Q cannot be

Fig. 7. Crack front propagation vectors.

solved, and have to be found iteratively. In this work this is done using the bisection method [22].

When the one point formula [10] is employed, stress intensity factors at points Q can be evaluated using the expressions:

$$K_{\mathrm{I}}^Q = \frac{E}{4(1 - \nu^2)}\sqrt{\frac{\pi}{2r}}\Delta u_b^P$$

$$K_{\mathrm{II}}^Q = \frac{E}{4(1 - \nu^2)}\sqrt{\frac{\pi}{2r}}\Delta u_n^P \tag{17}$$

$$K_{\mathrm{III}}^Q = \frac{E}{4(1 - \nu^2)}\sqrt{\frac{\pi}{2r}}\Delta u_t^P$$

where the terms $\Delta u_n^P, \Delta u_b^P$ and Δu_t^P are projections of Δu^P the displacement evaluated at point P, on the local coordinate directions (i.e. normal, binormal and tangential) at the crack front. Computed K values are then smoothed by using an interpolation function along the crack front. The interpolation function $K(\eta)$ is chosen here to be Chebyshev polynomial [22], where η is the position along the crack front. In this way stress intensity factors values are not only smoothed but also determined at the geometrical points Q' along the crack front (see Fig. 7).

It is well known that the near crack tip stress field fields on which the expressions (17) for the stress intensity factor computation are generally accepted in regions along the crack front far away from any intersection with a free surface, in other words, where it can be assumed that a condition approximating to plane strain prevails. It has been shown (see for example Folias [23] or Benthem [24]) that in the vicinity of the intersection of the crack front and a free surface, the displacements are not $O(r)$. As a consequence of this, poor results are generally obtained when expressions (10) are used to compute K for nodes close to free surfaces. In order to overcome this problem, K values for points Q' at the crack tips are obtained here from the extrapolation of interior K-values using the same function $K(\eta)$ cited above.

4.2. Crack extension

The discrete amount Δa corresponding to a given number of load cycles ΔN at a crack front point where ΔK occurs can be computed in an approximate form from Eq. (10) as

$$\Delta a \approx C(\Delta K_{eq})^n \Delta N \tag{18}$$

where ΔK_{eq} is the cyclic value of the equivalent stress intensity factor that accounts for the combined effects of the mode I, II, and III cyclic loads. Employing the expression of K_{eq} proposed by Gerstle [25], the resultant expression for ΔK_{eq} is

$$\Delta K_{eq}^2 = (\Delta K_{\mathrm{I}} + B|\Delta K_{\mathrm{II}}|)^2 + 2\Delta K_{\mathrm{II}}^2 \tag{19}$$

The S-criterion introduced in Section 3.2 is used to calculate the local direction of crack growth. For each point on

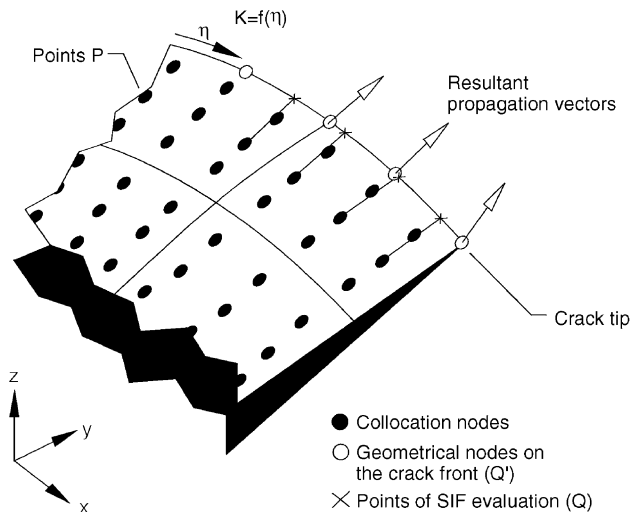the crack front (points Q in Fig. 7) the stationary point of $S(\theta)$ is calculated by solving expression (13) using the bisection method numerically and $S_{\min}$ is obtained by comparing the values of $S(\theta)$ at stationary points $d^2S(\theta)/d\theta^2 > 0$. The resultant propagation directions can then be referred to the global system of coordinates and expressed as propagation vectors $\vec{v}^Q$ with components (v_x^Q, v_y^Q, v_z^Q), as depicted in Fig. 7. It is worth noting that the procedure for determining propagation vectors at the crack front geometrical nodes Q' varies according to their particular location:

- For corner nodes shared by two crack front elements the propagation vector $\vec{v}^{Q'}$ is taken as the average of the propagation vectors of the two closest neighbouring points Q.
- For mid-side element nodes the propagation vector is taken equal to that at the closest point Q.
- For nodes located at the crack tips, the values of the components of the propagation vector $(v_x^{Q'}, v_y^{Q'}, v_z^{Q'})$ are

$$\{A\} \times [X] = [B]$$
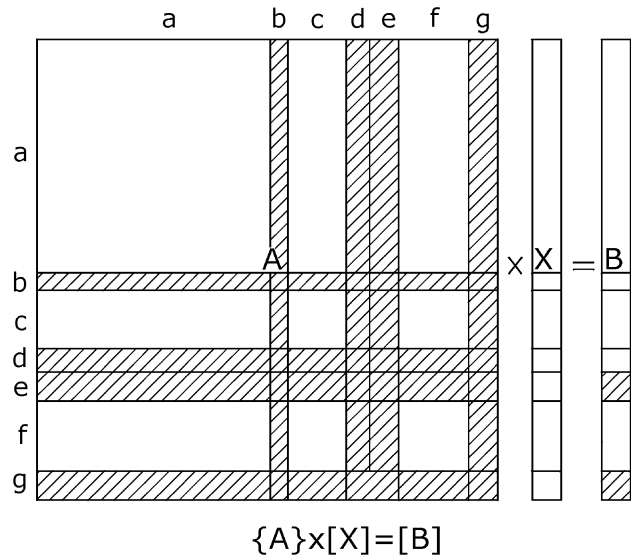
Fig. 9. Schematic representation of the system matrix assembling.
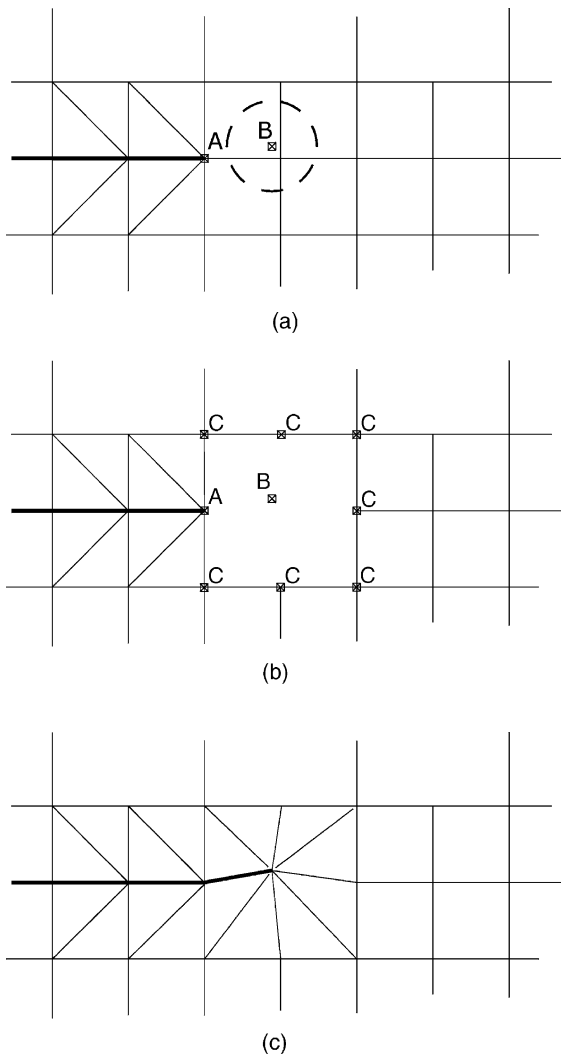

(a)

(b)

(c)

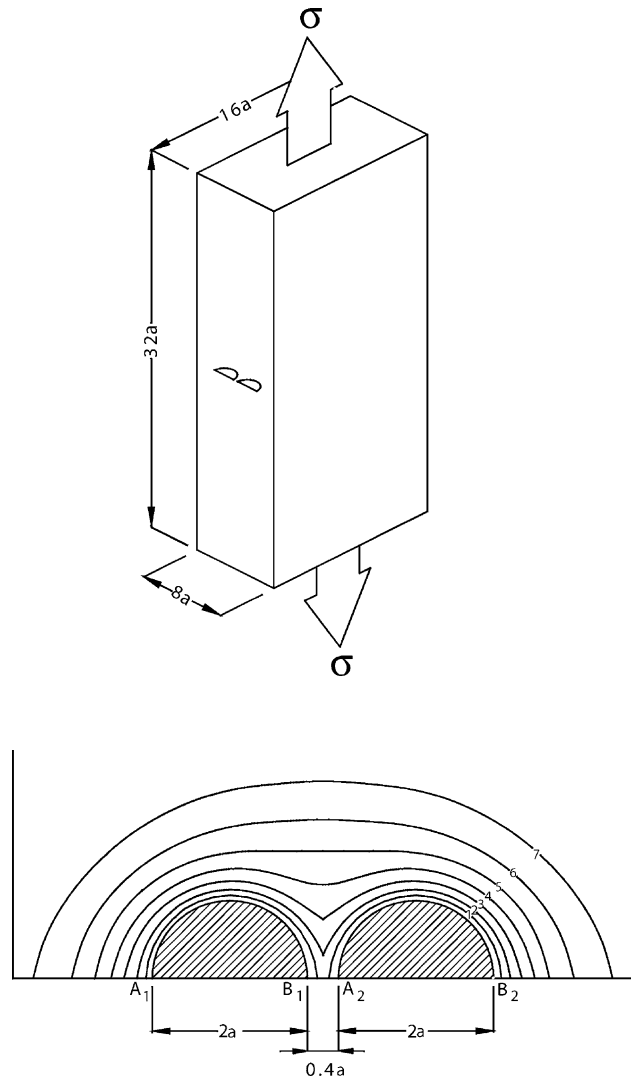Fig. 8. Crack tip remeshing procedure.

Fig. 10. A prismatic bar with two equal semicircular coplanar cracks under remote tension; model geometry and predicted crack shapes.
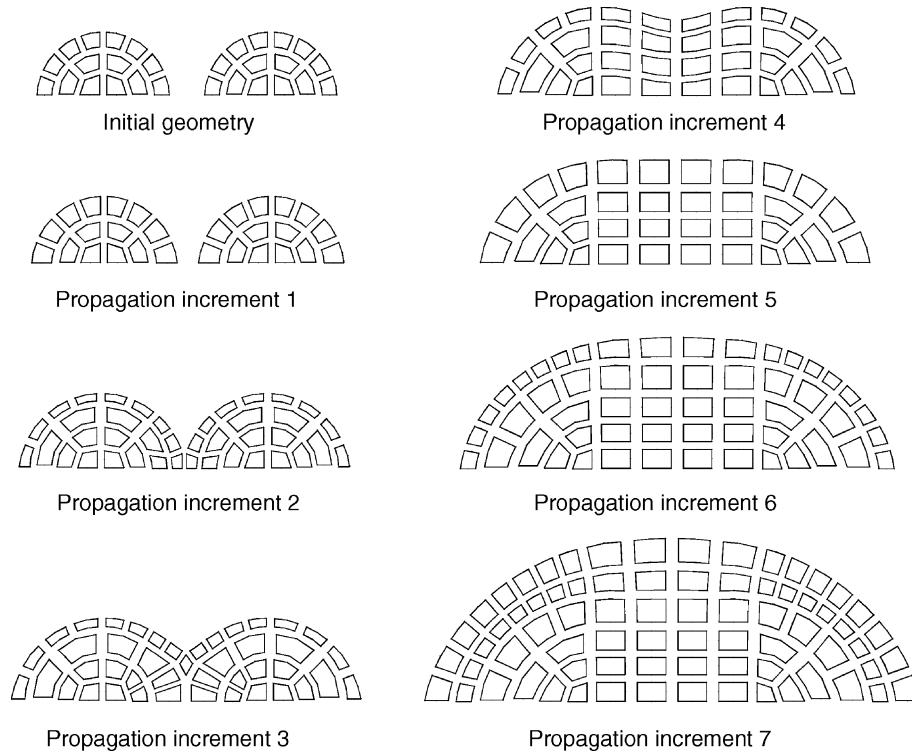
Fig. 11. Crack discretization of the twin coplanar cracks.

taken from the extrapolated values of the components of the propagation vectors of the interior points Q' and then projected onto the free surface plane.

4.3. Updating the model geometry and discretization

The strategy developed in this work for updating the model geometry consists of two parts The first is related to the crack extension a itself. This is simply done by adding new elements along the crack front, whose dimensions and orientations are, respectively, given by crack extensions Δa and propagation vectors $(v_x^{Q'}, v_y^{Q'}, v_z^{Q'})$ computed at the geometrical points Q'.

The second part is concerned with the mesh modification at the crack tip areas. If we consider a crack tip area such as the one depicted in Fig. 8(a), it is easy to see that in general, after a given crack extension the new position of the crack tip (point B) will not coincide with an element node. Hence the local redefinition of boundary element mesh will be necessary. In order to tackle this problem, a local remeshing strategy has been devised. The remeshing strategy is shown in Fig. 8 and can be described as follows:

- After the new position for the crack tip is determined (point B), those elements located in the vicinity of it (dashed circle in Fig. 8(a)) are removed from the mesh.
- Those nodal positions defining the undiscretized patch are identified (points C in Fig. 8(b)).

- Points C together with the previous and actual positions of the crack tip (points A and B, respectively) are employed for the discretization of the tip area into triangles by using the Delauny algorithm [26] (see Fig. 8(c))
- Vertices of the resulting triangles are then used to define discontinuous triangular elements, such as those introduced in Section 2.2. The use of discontinuous elements makes the approach general, since no care has to be taken regarding the common nodes at crack edges.
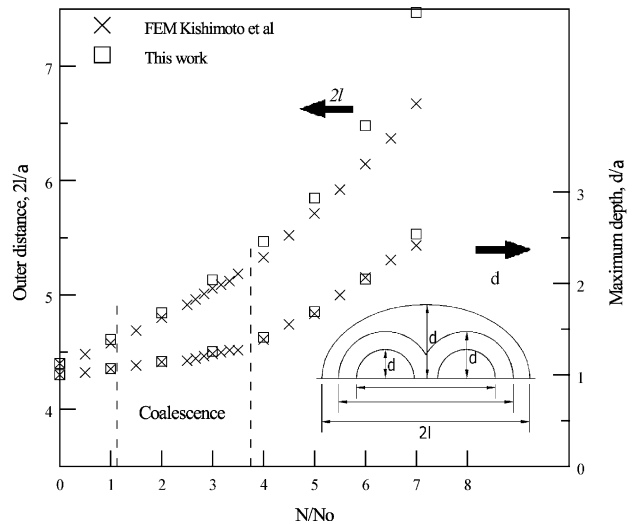

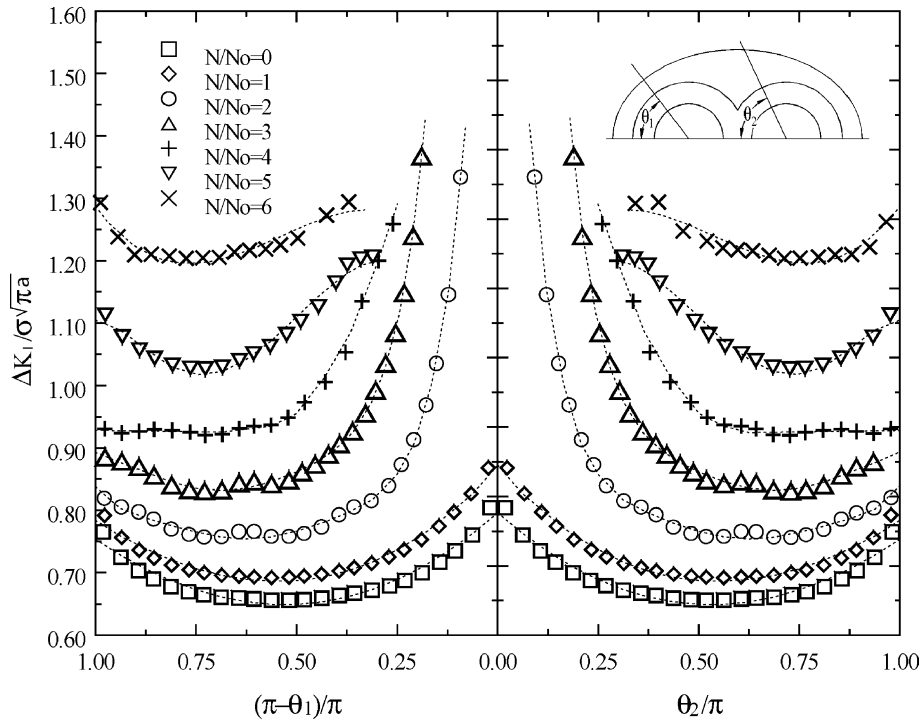Fig. 12. Crack growth curves predicted using FEM and BEM.

Fig. 13. Variation of ΔK_I along the crack fronts for each propagation step.

This strategy, which accommodates the required local mesh modifications into the existing model discretization, minimises the extra computation necessary to solve the new configuration; it is also suitable for the automatic simulation of multiple cracks approaching each other.

4.4. Updating the system matrix

It is easy to see that after each crack extension analysis, the rediscretization strategy introduced in the previous section alters only a small portion of the model discretization Therefore, only a few elements in the boundary element system matrix (see Section 2.3) need to be updated in order to solve the new configuration.

According to the sketch of the system matrix given in Fig. 9, matrix elements can be identified as:

a: nodes belonging to quadrilateral elements that have been unaffected by the rediscretization process,
b: nodes still present in the new discretization but which in the previous discretization were shared with elements that have been removed (nodes C in Fig. 8(b)),
c: nodes on the previous crack surfaces, except those located on the crack fronts,
d: nodes located on the old crack front elements,
e: nodes belonging to the new crack front elements,
f: nodes belonging to triangular elements which have not been affected by the rediscretization process,
g: nodes belonging to the new triangular elements added to the model.

Of all the listed matrix entries, only those in the hatched areas have to be updated, since they belong to elements that have been altered during the model rediscretization. Note that although the geometry of the old crack front elements is not altered during crack extension (they correspond to nodes labelled d), it is necessary to recalculate their entries since in the new analysis they are considered as standard discontinuous elements.
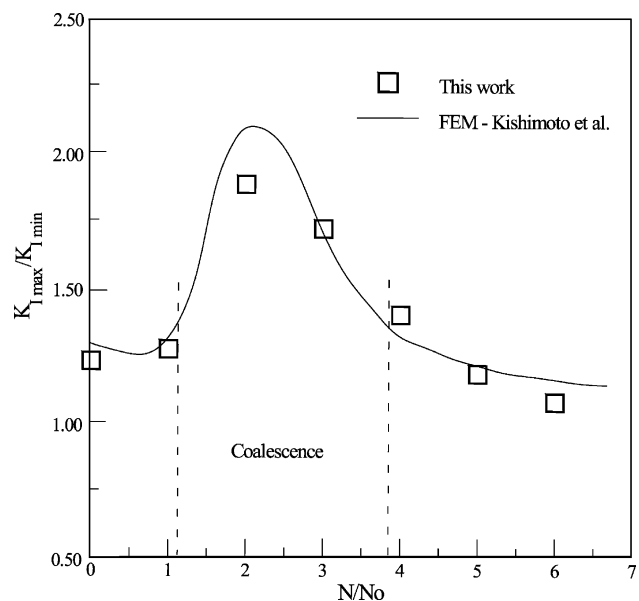

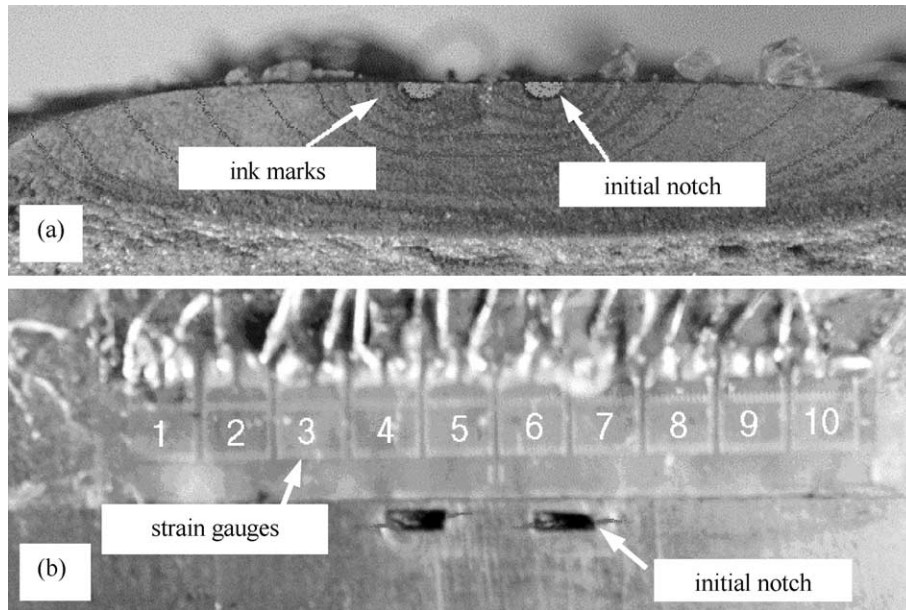Fig. 14. Evolution of $K_\mathrm{max}/K_\mathrm{min}$ along the crack front.

Fig. 15. Crack surface and top view of the specimen.

5. Examples

In this section a number of examples involving the propagation of multiple fatigue cracks are presented in order to demonstrate the capabilities of the proposed procedures. For each of the examples the evolution of the crack geometries and the stress intensity factors along the crack fronts during the propagation process are reported. Effects of crack interaction and coalescence are also analysed and compared with experimental observations.

5.1. Two equal coplanar semicircular

This first example consists of a prismatic bar containing two identical and symmetrical coplanar semicircular cracks of radius a Specimen dimensions scaled to the original crack radius a are shown in Fig. 10. The initial distance between the two adjacent crack tips (B_1 and A_2) in Fig. 10 was fixed equal to $0.4a$. The bar was subjected to a remote tensile stress σ at its ends, and the following Paris law was employed to estimate the crack growth:

$$\frac{\Delta a}{\Delta N} = 3 \cdot 10^{-11} \Delta K^{2.92} \qquad (20)$$

The evolution of the crack shapes is shown in Fig. 10 for seven propagation increments. The crack profiles in Fig. 10 are such that the same number of loading cycles, ΔN was taken to develop from one contour to the next. The reference number of cycles ΔN_0 was fixed at 750 cycles. Crack coalescence took place between the first and second propagation increments, and the transition from two cracks to one was assumed to occur when the cracks overlapped.

Fig. 11 shows the crack discretization for the initial configuration and the seven propagation increments. Crack growth curves for the outer distance and maximum depth are given in Fig. 12, where they are compared with those obtained by Kishimoto et al. [27] using finite elements. Very good agreement is found is general between the computed results and those from the reference, which differ only in for the outer distance value in the last propagation increments.

The stress intensity factors ΔK_I for the growing cracks are shown in Fig. 13. For each crack, normalized values of the stress intensity factors are plotted as a function of the angle between the horizontal axis and a radial line from the centre of the initial crack. It can be observed that the value of the stress intensity factor at adjacent crack tips increased as the cracks approached each other; it rapidly augmented at the contact zone during the early coalescence and it stayed high while the single crack shape was sharply concave. Finally it started to decrease as the crack adopted a regular front. The evolution of
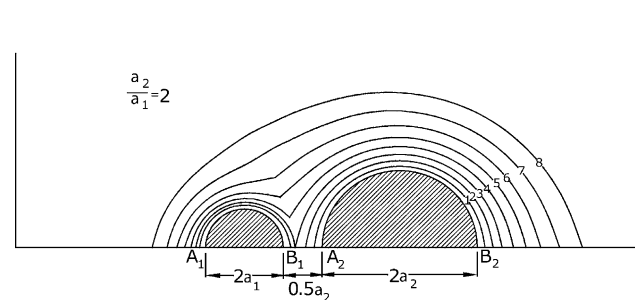

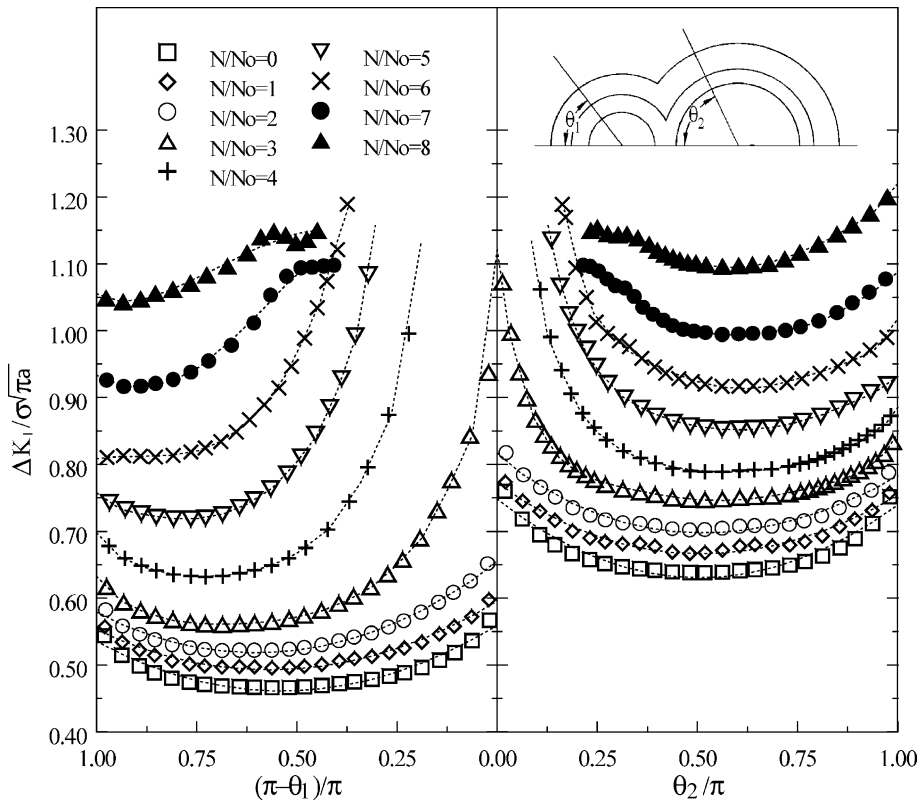Fig. 16. Predicted crack profiles for the second example.

Fig. 17. Variation of ΔKI along the crack fronts for each propagation step.

the $\Delta K_{max}/\Delta K_{min}$ is plotted in Fig. 14 together with results reported by Kishimoto et al. [27]. As can be seen, this ratio also reached its maximum value during coalescence, after which it started to decrease tending towards one, i.e. an iso-K configuration.

Fig. 15 depicts crack propagation in a typical weld specimen tested at INTEMA within the framework of the European Community Project INCO DC 950956 'High Performance Computing Simulation for Structural Integrity Analysis'. Fig. 15(a) shows a post-mortem view of a fracture surface in which the initial notches, as well as ink marks showing the evolution of the crack shape can be seen, while Fig. 15(b) corresponds to a top view of the specimen showing the strain gauge set-up used to monitor crack propagation [28]. Although the modelled example does not correspond exactly to the depicted experiment, it is worth to note that results in Figs. 10 and 15 show the same qualitative behaviour providing further evidence to validate the numerical model.

5.2. Two dissimilar and coplanar semicircular cracks

Consider now the analysis of two dissimilar coplanar cracks in a specimen with the same characteristics as those of the first example. The radii of the cracks are such that the radius of the small crack (a_1) is half of the large one ($a_2 = 2a_1$), to which all dimensions of the example are
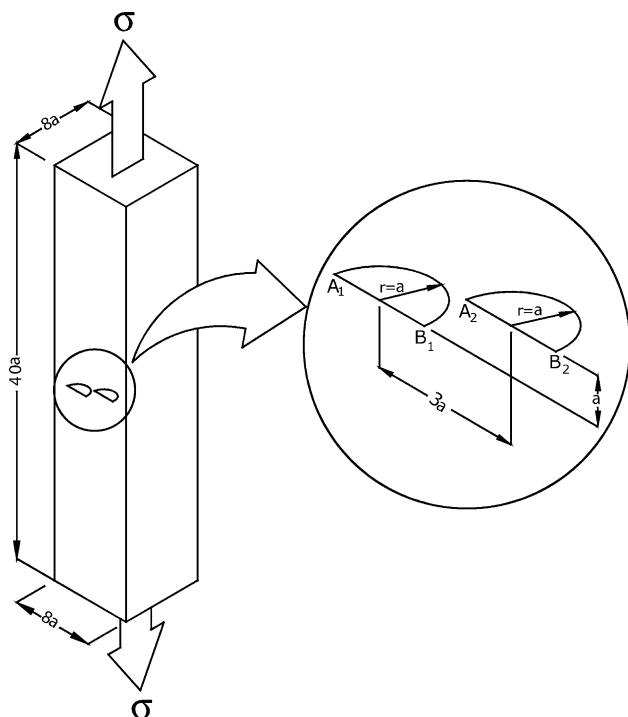

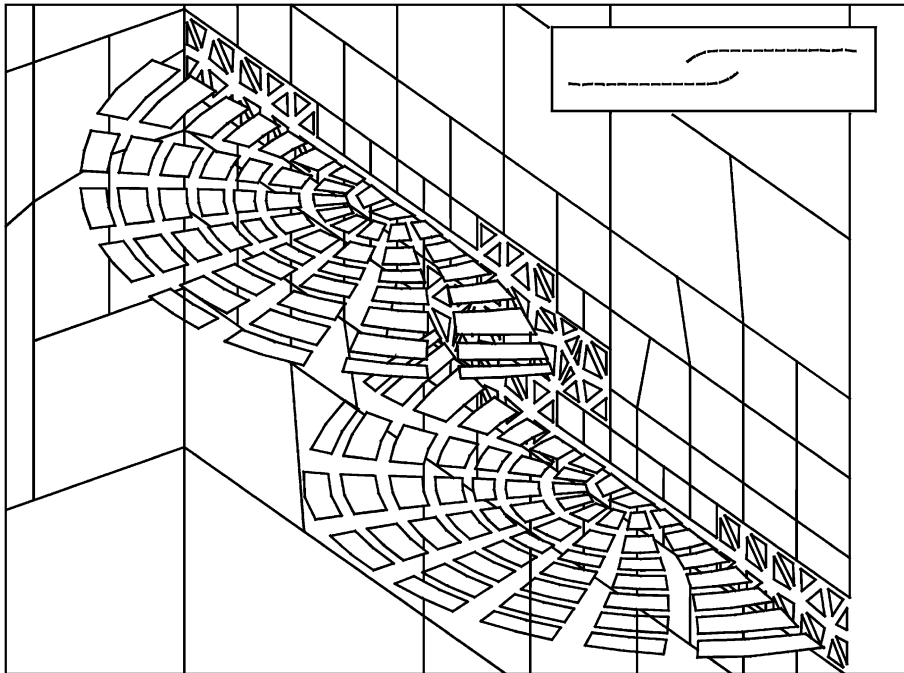Fig. 18. A prismatic bar with two semicircular, out-of-plane parallel cracks under remote tension.

Fig. 19. Predicted crack profiles for the third example.

referred. The initial distance between the closest crack tips (B_1 and A_2 in Fig. 16) was fixed to be half the initial radius of the large crack. The same material properties and propagation law were chosen as for the first example. Fig. 16 shows the evolution of the crack profiles for eight propagation increments, while the evolution of the mode I stress intensity factor along the crack fronts is presented in Fig. 17. The general behaviour in the evolution of the crack shape and stress intensity factor results are found to be similar to those of the first example.

5.3. Two offset semicircular parallel cracks

In this example, the case of a prismatic bar containing two identical offset semicircular parallel cracks is considered. Dimensions of the bar as well as the relative positions of the cracks scaled to the crack radius a are shown in Fig. 18. The bar was subjected to a remote tensile stress σ at its ends and crack growth estimated using the same Paris law as in the previous examples.

Fig. 19 is a rear view of the specimen where some of the boundary elements on its lateral face have been removed to show the cracks more clearly. Crack geometries correspond to those resulting after five propagation increments. In this example the reference number of cycles ΔN_0 was fixed at 3000 cycles and the propagation increments were not constant. Also shown in Fig. 19 are the discontinuous triangular elements introduced to the model during the automatic model rediscretization procedure. The sub-figure

in the top right-hand corner shows the crack propagation on the free surface.

The results obtained are in good agreement with the general behaviour reported by Soboyejo et al. [29] in their experiments; for a specimen of similar characteristics they also noted a deviation of the adjacent cracks tips as they approached each other (see Fig. 20). The same behaviour was observed for the tests carried out at INTEMA. The photograph in Fig. 21 depicts the propagation process of two misaligned cracks where it is clear how the adjacent tips pass each other before coalescence.

The evolution of the stress intensity factor components $\Delta K_I, \Delta K_{II}$ and ΔK_{III} are plotted for both cracks in Figs. 22–24. Since cracks propagated out of plane it was no longer suitable to represent the position on the crack front as a function of the angle θ as before. In this example position on the crack front is represented by the normalized
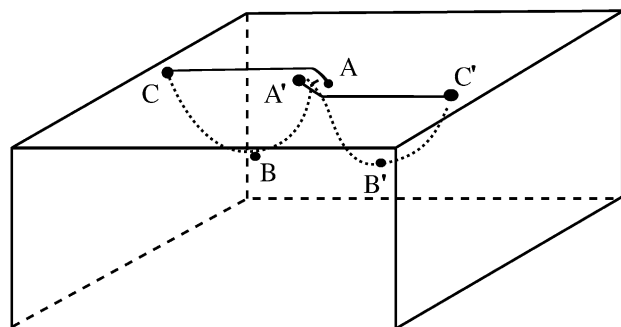

Fig. 20. Deviation of adjacent crack tips before coalescence. Schematic illustration (after Soboyejo et al. [29]).
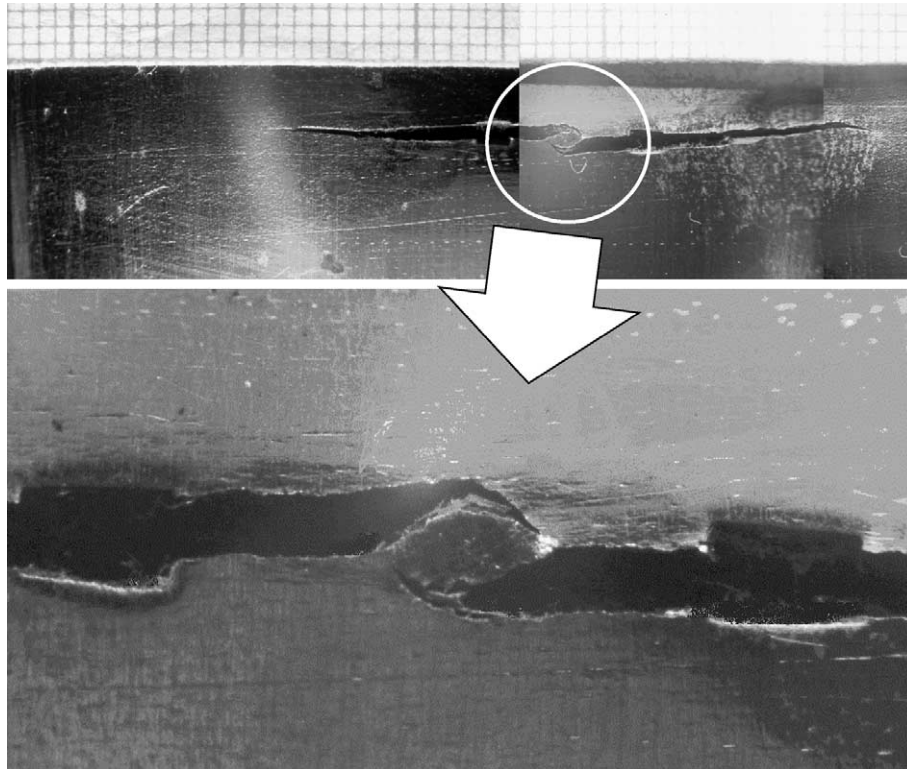
Fig. 21. Top view of specimen showing deviation of adjacent crack tips before coalescence.

distance given by the ratio of the distance η measured from the A_i crack tips (see Fig. 18) over the total crack front length l. Figures show that the behaviour of ΔK_I was almost unaffected by the presence of the second crack for the two first propagation increments. This was not the case

after the third increment, however, when the adjacent tips passed each other and a shielding effect took place occasioning ΔK_I values to dramatically decrease. In contrast to ΔK_I, ΔK_{II} values were early influenced by the presence of the second crack. Their absolute values
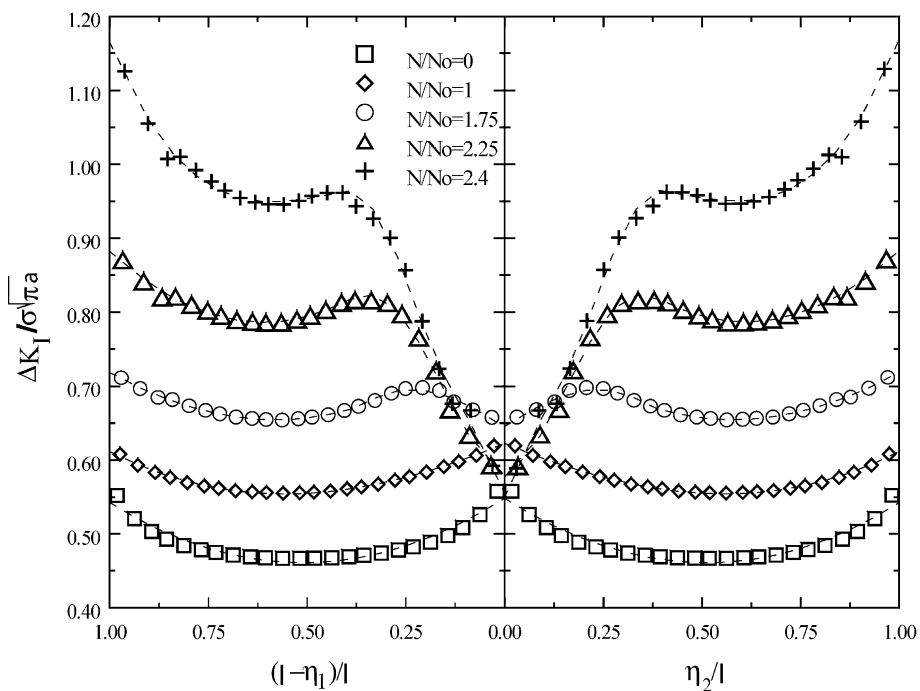

Fig. 22. Variation of ΔK_I along the crack fronts for each propagation step.
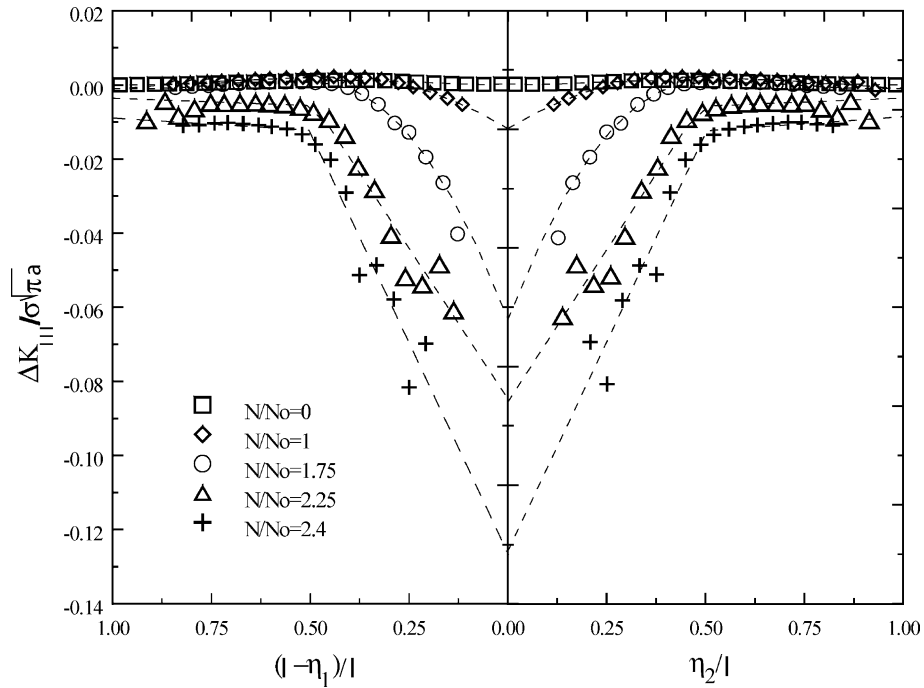
Fig. 23. Variation of Δ_{KII} along the crack fronts for each propagation step.

achieved a maximum to start with and decreased after the second crack extension. Note that the asymmetric evolution in the values of ΔK_{II} made the cracks grow towards each other. On the other hand the absolute value ΔK_{III} monotonously increased throughout the propagation process. However, these values are small when compared to ΔK_{I} and are hence not significant.

6. Conclusions

A DBEM procedure for the simulation of three-dimensional multiple fatigue crack growth and interaction has been presented in this paper. The paper has provided descriptions of the DBEM formulation, its discretization strategy and stress intensity factors calculation.
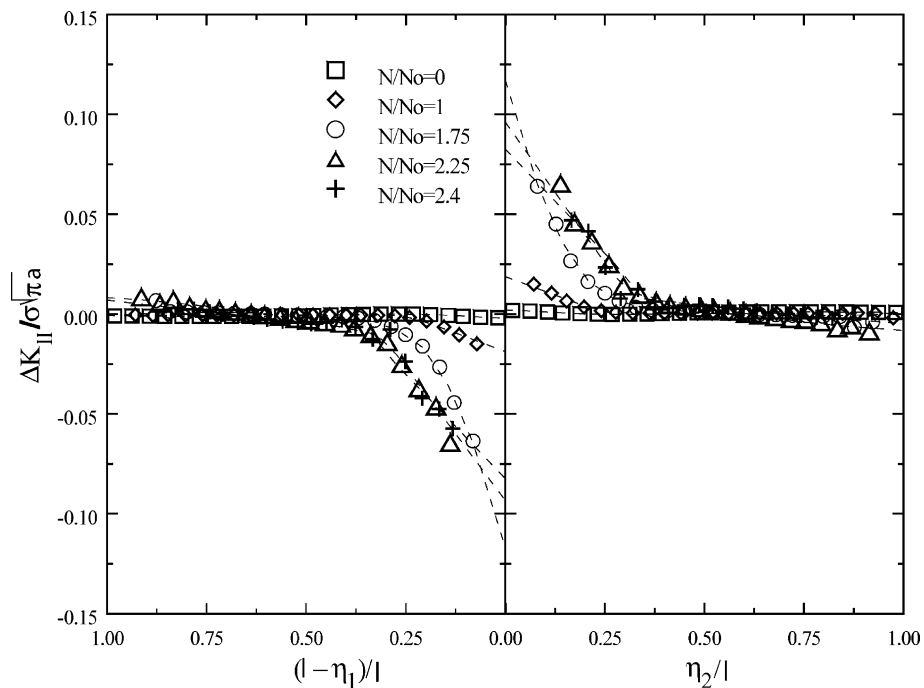

Fig. 24. Variation of ΔK_{III} along the crack fronts for each propagation step.

The DBEM single region analysis has proved to be particularly suitable for solving multiple crack problems, facilitating the construction of the model and its remeshing after each crack extension. Crack propagation is modelled using an incremental crack extension analysis based on the strain energy criterion and the Paris law. For each crack extension the DBEM is used to solve the model and the crack tip stress intensity factors K are computed from the crack opening and sliding displacements. Crack extensions are then automatically modelled with the introduction of new boundary elements along the crack fronts and a localized rediscretization in the area where cracks intersect the free surfaces. The devised localized remeshing strategy is robust and accommodates model changes in the original system matrices allowing for important savings in computing time.

The procedure was successfully employed to model the interaction and coalescence of coplanar and non-coplanar surface fatigue cracks. Obtained results are in agreement with experimental observations.

Appendix A

The Kelvin fundamental solutions $u_{ij}^*(x', x)$ and $t_{ij}^*(x', x)$ for the displacement boundary integral Eq. (1) are

$$u_{ij}^*(x', x) = \frac{1}{16\pi(1 - \nu)\mu r}[(3 - 4\nu)\delta_{ij} + r_{,i}r_{,j}] \quad (A1)$$

and

$$t_{ij}^*(x', x) = \frac{-1}{8\pi(1 - \nu)r^2}\left\{[(1 - 2\nu)\delta_{ij} + 3r_{,i}r_{,j}]\frac{\partial r}{\partial n} - (1 - 2\nu)(r_{,i}n_j - r_{,j}n_i)\right\} \quad (A2)$$

where $n = (n_1, n_2, n_3)$ is the outward normal at the field point x, and $r = r(x', x)$ represents the distance between the load point x' and the field point x, and its derivatives $r_{,i} = r_i/r$ are taken with reference to the coordinate of x.

Expressions for the fundamental solutions $U_{ijk}^*(x', x)$ and $T_{ijk}^*(x', x)$ present in the traction boundary integral Eq. (2) are

$$U_{ijk}^*(x', x) = \frac{1}{8\pi(1 - \nu)r^2}[(1 - 2\nu)(\delta_{ij}r_{,k} + \delta_{ik}r_{,j} - \delta_{jk}r_{,i}) + 3r_{,i}r_{,j}r_{,k}] \quad (A3)$$

and

$$T_{ijk}^*(x', x) = \frac{\mu}{4\pi(1 - \nu)r^3}\left\{3\frac{\partial r}{\partial n}[(1 - 2\nu)\delta_{ij}r_{,k} + \nu(\delta_{ik}r_{,j} + \delta_{jk}r_{,i}) - 5r_{,i}r_{,j}r_{,k}]3\nu(n_i r_{,j}r_{,k} + n_j r_{,i}r_{,k}) + (1 - 2\nu)(3n_k r_{,i}r_{,j} + n_j \delta_{ik} + n_i \delta_{jk}) - (1 - 4\nu)n_k\delta_{ij}\right\}, \quad (A4)$$

respectively.

References

[1] Nguyen TN, Wahab MA. A theoretical study of the effect of weld geometry parameters on fatigue crack propagation life. Engng Fract Mech 1995;51(1):1–18.

[2] Chapetti MD, Otegui JL. Controlled toe waviness as a means to increase fatigue resistance of automatic welds in transverse loading. Int J Fatigue 1997;10:667–75.

[3] American Society of Mechanical Engineers, Rules for in-service inspection of nuclear power plant components. ASTM boiler and pressure vessel code section XI div., 1; 1980.

[4] British Standard Institution, Guidance on some methods for the derivation of acceptance levels for defects in fusion welded joints. BSI PD6493; 1991.

[5] Tu ST, Dai SH. An engineering assessment of multiple crack growth of irregularly oriented cracks. Fatigue Fract Engng Mat Struct 1994; 17(10):1235–46.

[6] American Petroleum Institute, API recommended practice 579, 1st ed. Fitness for service; 2000.

[7] Cruse TA. Numerical evaluation of elastic stress intensity factors by the boundary integral equation in the surface crack: physical problems and computational solutions, ASME, New York 1972; 153–70.

[8] Portela A, Aliabadi MH, Rooke DP. The dual boundary element method: effective implementation for crack problems. Int J Num Meth Engng 1992;33:1269–87.

[9] Brebbia CA, Domínguez J. Boundary elements: an introductory course. Southampton/London: Computational Mechanics Publications/Mc-Graw Hill Company; 1992.

[10] Aliabadi MH, Rooke DP. Numerical fracture mechanics. Southampton/UK: Computational Mechanics Publications/Kluwer Academic Publishers; 1992.

[11] Mi Y, Aliabadi MH. Dual boundary element meted for three-dimensional fracture analysis. Engng Anal Boundary Elements 1992; 10:161–71.

[12] Cisilino AP, Aliabadi MH. Three-dimensional BEM analysis for fatigue crack growth in welded components. Int J Press Ves Piping 1997;70:135–44.

[13] Cisilino AP. Linear and nonlinear crack growth using boundary elements. Topics in engineering, vol. 36. Southampton, UK: WIT Press; 2000.

[14] Lachat JC, Watson JO. Effective numerical treatment of boundary integral equations: a formulation for three-dimensional elastostatics. Int J Num Meth Engng 1976;10:991–1005.

[15] Rizzo FJ, Shioppy DJ. An advanced boundary integral equation method for three-dimensional thermoelasticity. Int J Num Meth Engng 1977;11:1753–68.

[16] Guiggiani M, Krishnasamy G, Rizzo FJ, Rudolphi TJ. Hypersingular boundary integral equations. In: Morino L, Piva R, editors. A new approach to their numerical treatment, in boundary integral methods, theory and applications. Berlin: Springer-Verlag; 1991. p. 211–20.

[17] Aliabadi MH, Hall WS, Phemister TG. Taylor expansions for singular kernels in the boundary element method. Int J Num Meth Engng 1985; 21:2221–36.

[18] Mi Y, Aliabadi MH. Dual boundary element method for three-dimensional fracture analysis. Engng Anal Boundary Elements 1992; 10:161–71.

[19] Paris PC, Gomez MP, Anderson WP. A rational analytic theory of fatigue. The trend in engineering 1961;13:9–14.

[20] Sih GC. Mechanics of fracture initiation and propagation. London: Kluwer Academic Publishers; 1991.

[21] Elber W. Fatigue crack closure under cyclic tension. Engng Fract Mech 1970;29:37–45.

[22] Press WH, Flannery BP, Teukolsk SA, Velterling WT. Numerical recipes. Cambridge, UK: Cambridge University Press; 1986.

[23] Folias ES. Method of solution of a class of three-dimensional elastostatic problems under Mode I loading. Int J Fract 1980;16:335–48.

[24] Benthem JP. State of stress at the vertex of a quarter-infinite crack in a half space. Int J Solids Struct 1977;13:479–92.

[25] Gerstle WH. Finite and boundary element modelling of crack propagation in two- and three-dimensions using interactive computer graphics. PhD Thesis, Cornell University, Ithaca, NY, USA; 1986

[26] Sloan SW. A fast algorithm for constructing Delaunay triangulations in the plane. Adv Engng Software 1987;9(1):39–55.

[27] Kishimoto K, Soboyejo WO, Smith RA, Knott JF. A numerical investigation of the interaction and coalescence of twin coplanar semi-elliptical fatigue cracks. Int J Fatigue 1989;11(2):91–6.

[28] Otegui JL, Mohaupth UH, Burns DJ. Strain gauge technique for monitoring small fatigue cracks in welds. Engng Fract Mech 1991; 40(3):549–70.

[29] Soboyejo WO, Knott JF, Walsh MJ, Cropper KR. Fatigue crack propagation of coplanar semi-elliptical cracks in pure bending. Engng Fract Mech 1990;37(2):323–40.